CHALMERS
UNIVERSITY OF TECHNOLOGY

Temporal Variations in L-band Reflectivity Profiles of a Boreal Forest During Growth and Drought

Citation for the original published paper (version of record):
Bennet, P., Monteith, A., Ulander, L. (2026). Temporal Variations in L-band Reflectivity Profiles of a Boreal Forest During Growth and Drought. IEEE Journal of Selected Topics in Applied Earth Observations and Remote Sensing, 19: 16299-16313.
http://dx.doi.org/10.1109/JSTARS.2026.3690549

(article starts on next page)

Temporal Variations in *L*-Band Reflectivity Profiles of a Boreal Forest During Growth and Drought

Patrik J. Bennet, Albert R. Monteith, and Lars M. H. Ulander, *Fellow, IEEE*

***Abstract*—Forest water dynamics related to vitality, such as tree water stress and transpiration, modulates the forest's microwave reflectivity, but the connections have not yet been established, leaving unexplored potential for satellite missions. This study presents and models time series of *L*-band reflectivity and attenuation observed by a multipolarization tomographic radar in a *Picea abies* L. Karst (Norway spruce) stand during a growth season subject to drought. Temporal phenomena in reflectivity are found, with surprising differences between polarizations and with characteristics shifting over time-scales of weeks. Diurnal cycles of 0.5 to 1 dB were often present in HH and VV canopy intensity (reflectivity above 4 m height), not necessarily simultaneously, with opposite phase. A model is formulated that describes the reflectivity profile as a combination of microwave scattering and extinction profiles. Model-estimated scattering is found more strongly linked to forest water dynamics than the observed canopy intensity. During the drought, coefficient of determination (R^2) values of VV canopy scattering and intensity are 0.70 and 0.43 for diurnal variations with vapor pressure deficit, a driver of transpiration, and 0.92 and 0.75 for daily averages with soil moisture (SM), indicating tree water stress. The daily average HV ground scattering and intensity show R^2 values of 0.81 and 0.29 with SM over the growth period. This study shows that a combination of microwave extinction and scattering can explain the reflectivity phenomena, and can be decomposed by model-based estimation via radar tomography and attenuation measurements, producing more direct relations to tree water stress and transpiration.**

***Index Terms*—Attenuation, boreal forest, drought, *L*-band, radar tomography, time series.**

I. Introduction

REMOTE sensing of forest health and vitality is increasingly in demand by both climate scientists and foresters [1], [2], [3]. Current trends in global climate are predicted to make heatwaves and drought more common, not least in boreal forests [4], and may affect previously considered tolerant or not-at-risk forests with unexpected force [3]. Meanwhile, forests play a key role in the global carbon and hydrological cycles, and modulate the global energy balance [1], [5]. Radar observations have shown signatures related to forest transpiration and water stress [6], [7], [8], which motivates exploration of the prospects to measure such quantities with radar. The BorealScat tower radar experiment has provided us with unique observations of a boreal forest as it experienced drought, which triggered an infestation of *Ips typographus* (European spruce bark beetle), with temporal variations measured in unprecedented detail [9], [10], [11].

Radar observations of natural environments are highly sensitive to water, as it dominates the dielectric properties of ground, atmosphere, and vegetation, modulating the reflectivity [12]. Trees transport water from the ground, store it in their stems and exchange it with the atmosphere as they bind carbon through transpiration [13]. High transpiration during the day depletes the stem water storage, a process partly driven by vapor-pressure deficit (VPD) and regulated by stomatal closure, and it replenishes during the night. It has been hypothesized in previous studies that diurnal variations in radar reflectivity are caused by this biophysiological process [11], [14]. The water dynamics in a forest is strongly connected to its health and vitality, e.g., with drought-induced tree water stress making the trees susceptible to xylem cavitation or insects [13], [15]. This motivates research on radar as an instrument to observe forest water dynamics and thereby health and vitality.

Satellite synthetic aperture radar (SAR) operating at *L*-band is attractive for forest observations, constituting a tradeoff between signal penetration, resolution, and antenna size considerations. Ground-based radar tomography experiments are tools for building a detailed understanding of the satellite observations and for exploring the potential of new missions. That is, of *L*-band SAR satellite missions, such as SAOCOM-1, ALOS-2/4, the recently launched LuTan-1 and NISAR missions, the planned ROSE-L satellite, and the under evaluation SAOCOM-CS mission, with later development toward interferometric/tomographic capabilities [16], [17], [18], [19], [20], [21]. Furthermore, the proposed SLAINTE mission advocates subdaily *L*-band observations for monitoring ecosystem health [22].

Radar tower experiments are currently the only platforms enabling analyses of temporal variations in forest radar observations on time scales of seconds to years [9], [10], [11], [14], [23], [24], [25], [26], [27], [28]. Furthermore, the forest reflectivity is a result of complex electromagnetic scattering mechanisms [29], [30]. A tomographic radar is able to isolate effects of these mechanisms by resolving the reflectivity in height, enabling the separate analysis of forest canopy and ground components [31]. Radar observations suffer from speckle noise, demanding significant averaging to yield precise radiometric resolution. This is particularly important for reliable measurement of the up to 1 dB diurnal variations in forest canopy reflectivity,

Received 14 November 2025; revised 13 February 2026 and 31 March 2026; accepted 18 April 2026. Date of publication 5 May 2026; date of current version 21 May 2026. This work was supported in part by Hildur and Sven Wingquist Foundation for Forest Research, in part European Space Agency (ESA), and in part by Swedish National Space Agency and Vinnova.

The authors are with the Department of Space, Earth and Environment, Chalmers University of Technology, 41296 Gothenburg, Sweden (e-mail: patrik.bennet@chalmers.se).

Digital Object Identifier 10.1109/JSTARS.2026.3690549

as has been observed for P-band in both boreal and tropical forests [11], [14]. Radar tomography can be used to improve both these aspects. Measurements of the forest canopy attenuation provide information on the microwave extinction mechanism (i.e., the attenuation per distance), and hence, assist in separating the behaviors of microwave extinction and scattering when combined with observations of the canopy reflectivity.

In this study, we present tomographic radar time-series measurements at L-band, acquired by the BorealScat tower radar, over a *Picea abies* L. Karst (Norway spruce) stand during a growth season subject to drought; this caused an *Ips typographus* infestation, which became apparent in the following year, and most of the forest had to be felled. Thus, we were provided the unique opportunity to study the radar observation signatures of a boreal forest as it experienced water stress.

In order to understand these signatures, we need to have an idea of the dielectric variations in the forest. Studies of the spatio-temporal dielectric, radial, and sap flow variations in *P. abies* tree stems have been conducted [32], [33], [34], [35]. Based on their findings, we expect the radar observations to be modulated by stem water variations with stronger relative variations in the crown than at the stem base [32], [33], [35]. These modulations should be highly correlated with VPD, and also be affected by stomatal closure, which prevents stem water depletion especially during dry or warm periods where VPD exceeds 15 hPa [34]. Furthermore, the dielectric constant was observed larger at microwave polarization parallel, rather than perpendicular, to wood fibers [36], implying polarization differences in sensitivity to stem water.

Thus, this study aims to present the L-band time series measurements from the BorealScat experiment over the growth season subject to drought, and bring a qualitative understanding to the observed temporal phenomena, particularly in terms of forest water dynamics. In this process, in order to separate microwave scattering and extinction effects, we also formulate a microwave scattering model. The BorealScat experiment and data are described in Section II. In Section III, we present unique time series of multipolarimetric tomographic L-band radar reflectivity and canopy attenuation, during the growth season of 2018. In Section IV, a novel model-based approach for separating scattering mechanisms in the reflectivity profiles is evaluated. Finally, correlations of radar quantities with environmental parameters, i.e., VPD and soil moisture (SM), are quantified in Section V. Finally, Section VII concludes this article.

II. BorealScat Experiment and Data

This study presents measurements by the BorealScat tower radar over a mature *P. abies* stand located at Remningstorp in southern Sweden [10]. The experiment was conducted from 2017 to 2021. The forest was standing on flat terrain, with an above-ground biomass of about 250 tons/ha and tree heights of 25 to 27 m. The stand was about 56 years old in 2018, as its mean tree age was estimated to be 48 years during the 2010 BioSAR campaign [37]. Biomass was estimated within a 10 m diameter plot within the stand, where all trees with a diameter at breast height greater than 4 cm were calipered and the heights of 25% of the trees were measured. Above-ground biomass was estimated using allometric equations [38], and extended to plot-level using airborne lidar scans trained and validated on multiple plots in Remningstorp. Given the tree age and height, the biomass would not have increased significantly throughout the BorealScat experiment. The annual growth cycle of *P. abies* starts in April and ends by October [39], and this is the period we refer to as the growth season.

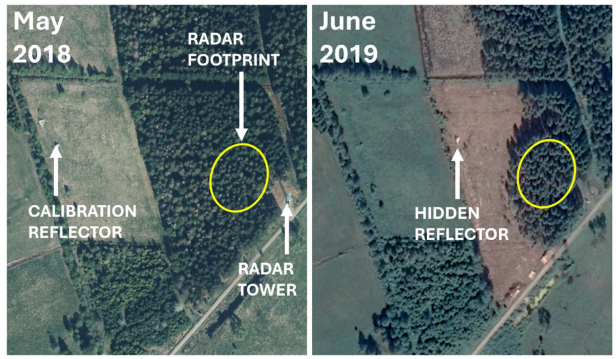

Fig. 1. Overview of the forest observed by the BorealScat tower radar. The leftmost image shows the area in May 2018, at the beginning of the period analyzed in this study. The rightmost image shows the area in June 2019, where the *Ips typographus* infested forest has been felled, revealing the hidden reflector in the forest. Images courtesy of Lantmäteriet and Google Earth. Note that the resolution and contrast are slightly worse in the 2019 image, making fine structures like the radar tower less discernible.

An overview of the forest stand observed in the experiment is shown in Fig. 1. Radar time series measurements were running between 2017 to 2021, with a gap in 2019 summer data. In this study, we focus on phenomena in the L-band measurements during the 2018 drought-affected growth season, that we hypothesize relate to the tree water dynamics.

A. BorealScat Tower Radar

The BorealScat P- and L-band radar consisted of an array antenna with 20 elements at the top of a 50 m high tower, connected through 60 m long low-loss cables to a 20-port vector network analyzer in a hut at its base [10]. A total of 10 antennas were used for horizontally (H) and 10 for vertically (V) polarized transmit/receive pairs, positioned such that a virtual vertical aperture provided resolution in elevation. A measurement done with vertical–vertical transmit–receive pairs is abbreviated as made at VV polarization, and similarly for the corresponding HH and HV combinations. P- and L-band measurements were done in sequence, with tomographic measurements taken every 5 min. At L-band, the center frequency was 1307.5 MHz with a bandwidth of 135 MHz. Details on the antenna array design, measurement sequences and calibration procedures are described in [9], [10], [40], [41], and [42].

The reflectivity observed by the radar is calibrated relative to an undetermined factor within each polarization channel [10]; differences between polarizations, therefore, cannot be compared in an absolute sense, i.e., relative variations over time are well calibrated, but there is an undetermined constant in the VV/HH intensity ratio.

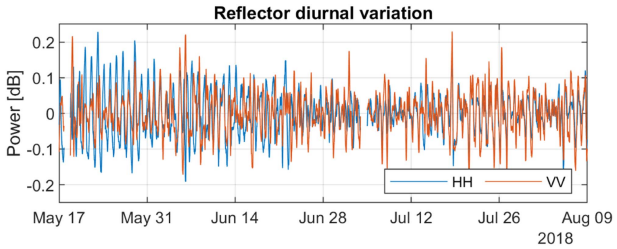

Fig. 2. Calibration reflector *L*-band backscatter variation around the 24 h mean power during summer 2018.

The main forest region of interest lies in 20 to 70 m ground range distance from the radar, covering a range of incidence angles about 20° to 55° along the ground. Speckle is reduced by averaging the intensity observed by the radar both spatially and temporally, by horizontal and vertical integration in the intensity tomograms as well as by applying an averaging window over time. The minimum number of looks is about 162 over the region of interest in a single *L*-band tomogram [42], and the statistical variations are then further reduced by the time averaging, which multiplies the number of looks in a single tomogram.

Two trihedral corner reflectors with 5 m short sides were placed in the scene, tilted up towards the radar: one at line-of-sight (LOS) in an open field at 200 m distance and one concealed under the forest canopy at 127 m distance in ground range from the radar. The reflector in the field was used to assess the radar system stability, while the concealed reflector (CR) was used to measure forest canopy attenuation.

Diurnal backscatter variations are small, typically on the order of 1 dB. Thus, it is crucial to quantify the systematic diurnal variation of the radar to avoid errors in interpreting the results. The variations around the daily average backscatter at the reflector in the field, smoothed over 4 h, is shown in Fig. 2, where the time series covers the growth season of 2018. It can readily be seen that the reflector variations overall are less than ±0.2 dB.

B. Bark Beetle Infestation

The forest stand became infested with *Ips typographus* during the course of the BorealScat experiment, triggered by the drought in 2018 studied in this article. Fig. 1 shows the forest stand in May 2018 and June 2019. A large part of the stand was felled in May 2019, as can be seen in the figure, due to the spreading *Ips typographus* infestation. Part of the forest was kept around the radar footprint, chosen such that the felling did not affect the forest region studied by the radar tower.

The tree deaths and damage within an 80 m radius around the radar tower were documented. The following data regards tree deaths (indicated by decay and loosening branches) due to *Ips typographus*, for an initial total of 460 living trees; 3% of the trees died in 2018; 13% of the remaining trees died in 2019; 14% of the remaining trees died in 2020. Most of the dead trees were located around the sunny edges of the forest stand, where intense sun and lower SM levels stresses the trees, making them more susceptible to the insects.

TABLE I
IN SITU SENSOR-COLLECTED ENVIRONMENTAL PARAMETERS

Parameter	Accuracy	Location
Air temperature	±0.4 °C	At ground level and at 30 m
RH	±8%	At ground level and at 30 m
Air pressure	±0.15 kPa	At ground level and at 30 m
SM	±3%	Within the forest stand
Precipitation	±4%	On the roof of the equipment hut
Mean wind speed	±1.3 m/s	Two sensors at the top of the tower

C. Canopy Attenuation

The attenuation of the radar signal as it propagates through the forest canopy is an important mechanism in radar observations of forests, as it modulates the returning reflectivity of scatterers within the forest. The canopy attenuation was measured by observing the CR, located at an incidence angle of 67° to the tower radar. More precisely, the two-way attenuation was measured by extracting the peak power over a small area around the reflector in the radar tomograms (acquired every 5 min) and smoothing it over 4 h (if not explicitly stated otherwise). Absolute calibration of the attenuation was done by normalizing the power level to that observed after the forest obstructing the reflector was felled in late May 2019, such that the CR was in LOS of the radar's antennas.

The CR peak power was more noisy at HH than at VV, due to more canopy attenuation at HH, reducing its signal-to-noise ratio (SNR). The attenuation measurements' noise-equivalent saturation level was estimated by observing a region at ground level 20 m behind the CR. The same procedure was carried out over this noise-region as at the CR, taking the peak value of the region as the noise-equivalent intensity.

D. Collected and Estimated Environmental Data

The in situ sensor-collected environmental data used in this study includes air temperature, relative humidity (RH), air pressure, SM, precipitation, and wind speed. The sensors accuracy and locations are summarized in Table I. Measurements were acquired every 5–10 min and, just like the radar observations, smoothed over 4 h. Air temperature, RH, and air pressure were collected by two sensors each, located at ground level and at 30 m height. In the case of two sensors, their mean values were used.

In addition, VPD was estimated from air temperature and RH as

$$\mathrm{VPD} = \frac{100 - \mathrm{RH}\,[\%]}{100}\mathrm{SVP} \tag{1}$$

where the Goff and Gratch (1945) formula for saturated vapor pressure (SVP) was used [43].

III. RADAR TOMOGRAPHY, CANOPY ATTENUATION, AND ENVIRONMENTAL PARAMETER TIME SERIES

The *L*-band reflectivity profiles' time series over the summer of 2018 are shown in Fig. 3, at HH, VV, and HV polarizations. The time period spans from May 17 to October 1, whereas the annual growth cycle of *P. abies* starts in April and ends by October [39]. Radar tomograms of the forest were acquired

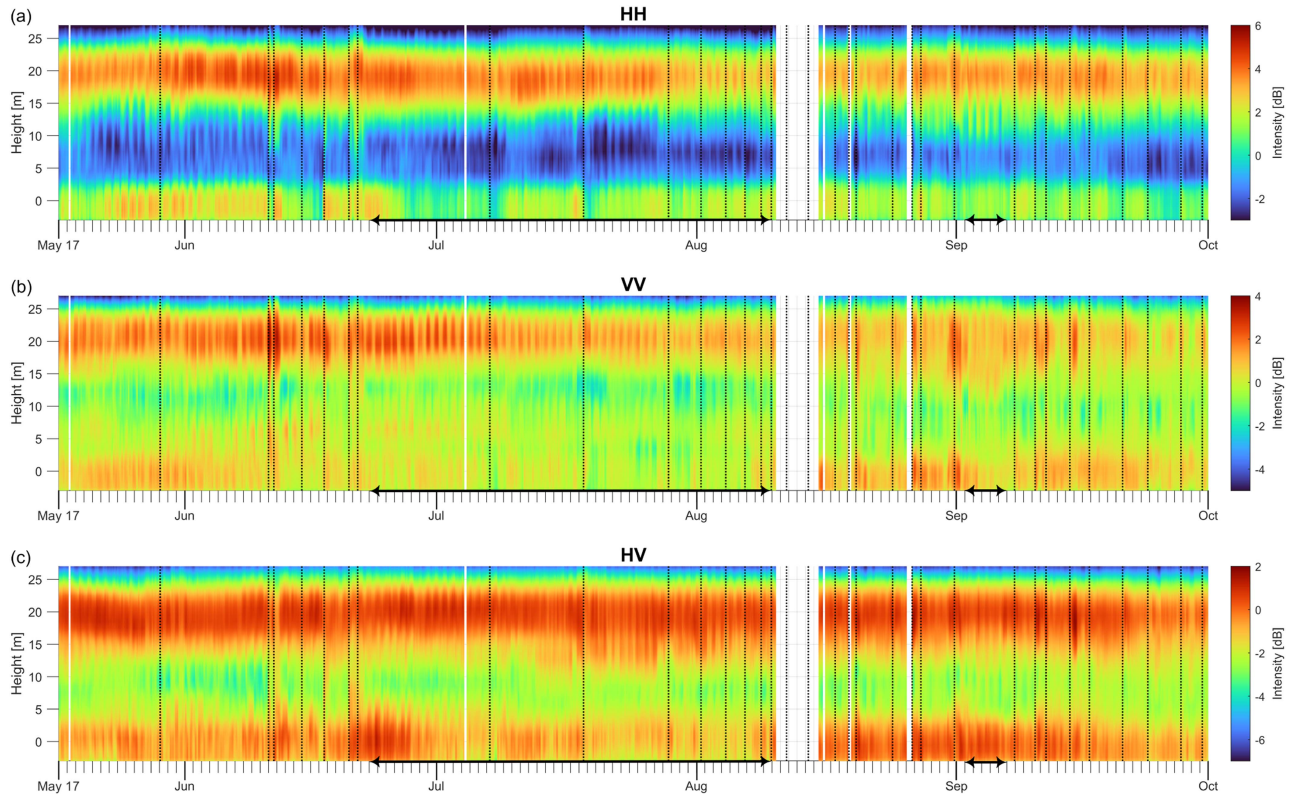

Fig. 3. *L*-band VRP time series from May 17 to October 1 2018, smoothed over 4 h temporally and 6 m vertically. The color scales span over 9 dB. The vertical dotted black lines indicate rain events, as shown in Fig. 4, and the black arrows on the time axis indicate the studied drought period in July to August and the precipitation-free time window in September.

every 5 min and reflectivity profiles were obtained by averaging the reflectivity from 20 to 70 m in ground range. The profiles were smoothed over 6 m in height and 4 h in time. The dotted black lines indicate rain events and July to August was a period of drought, as is indicated by the low SM level and absence of significant precipitation.

A canopy and ground intensity decomposition is shown in Fig. 4 over the time series, together with the total intensity, the measured two-way attenuation at the CR and the environmental parameters.

A. *Reflectivity Profiles Over the Growth Season*

The reflectivity profiles time series of Fig. 3 show different characteristics over time and height, as well as between polarizations. In general, the HH reflectivity is strong in the upper canopy and decreases significantly for decreasing height, and there is a clear ground response. There are diurnal cycles present, i.e., subdaily cycles repeated over many days, in May, early July to early August and for a few days in the beginning of September. The VV reflectivity is, just as at HH, strong in the upper canopy, but shows a more even vertical distribution than that at HH. Diurnal cycles can be seen in the upper canopy from May to the end of July. They are most apparent in late June and successively fade out during the drought period. At HV, there are indications of diurnal cycles in May, late June, and in late July, but they are less clear.

B. *Total, Canopy, and Ground Intensity*

The total intensity, i.e., as would be observed in a regular SAR image, and its canopy and ground intensity components are shown in Fig. 4. The canopy and ground intensity components were obtained as the integrated reflectivity above and below 4 m height, respectively, where the 4 m limit is chosen due to the resolution of the ground layer. All intensity levels in the figure are referenced to the average intensity of the total intensity at HH. The total intensity is dominated by the canopy intensity at all polarizations. Diurnal cycles and rain effects are more expressed in the canopy intensities than in the total intensity. At HH, diurnal cycles are also apparent in May and are starting earlier in July, continuing into August, with variations about 0.7 dB. The VV canopy intensity component is similar to the total intensity, but with slightly stronger variations. Diurnal variations up to 1 dB persist throughout late June to early July and fades as the drought continues. The HH and VV canopy intensities have decreased about 1 dB by the end of the drought period compared to at its start. Rain affects the canopy intensity similarly to the total intensity, but with larger variations. The ground intensity components at HH and especially at HV show common trends with the SM content.

C. *Canopy Attenuation*

The canopy two-way attenuation measurements are affected by noise and especially so at HH, which limits the ability to

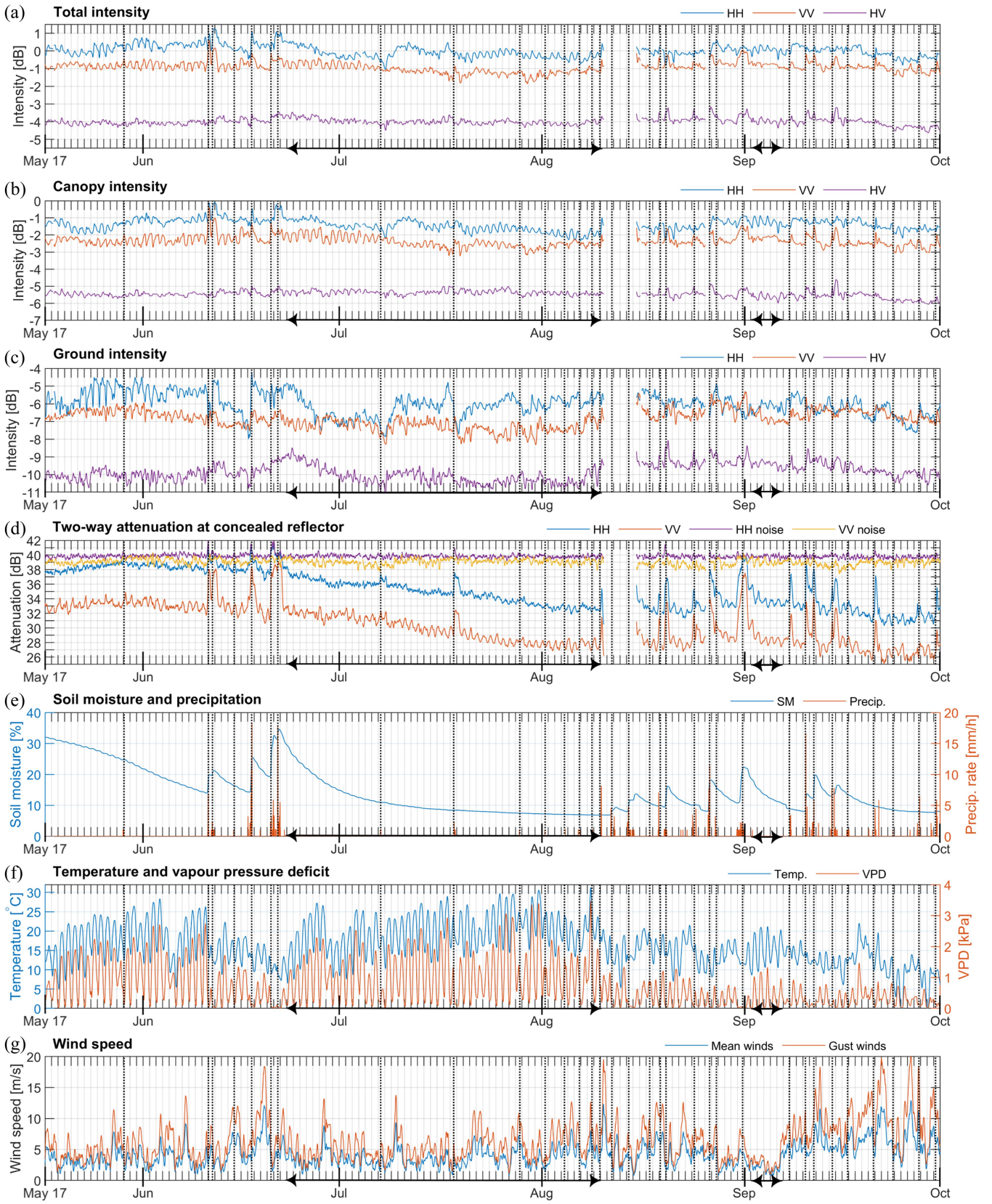

Fig. 4. Time series from May 17 to October 1 2018 of *L*-band multipolarimetric tomographic radar total intensity, canopy intensity (integral above 4 m height) and ground intensity (integral below 4 m height) in the *P. abies* stand. Intensity levels are referenced to the average power of the HH total intensity. Measured *L*-band canopy attenuation is also included, as well as SM, precipitation, temperature, and estimated VPD. All data are smoothed over 4 h and the time-axis' tick marks coincide with midnight. The vertical dotted black lines indicate the time of rain events, and the black arrows on the time axis indicate the studied drought period in July to August and the time window in September.

observe small diurnal variations. The absolute measured attenuation will be offset and saturated for a low SNR, making the measured attenuation an underestimation of the actual attenuation. Attenuation noise measurements are included in Fig. 4, obtained as described in Section II-C. The two-way attenuation (excluding precipitation effects) decreases about 6 dB over the season and the measurement quality has thus improved by the late growth season as the SNR has increased. These 6 dB may seem as a large effect, but note that the incidence angle at the reflector is 67°, corresponding to about 60 m propagation distance in the canopy and 0.1 dB/m attenuation decrease.

Notably, the two-way attenuation is about 4 to 5 dB larger at HH than at VV, which demonstrates a clear polarization difference. A decrease in attenuation is most apparent during the drought in late June to early August, with a 4 dB decrease, and attenuation variations (excluding diurnal cycles) seem to follow the SM content. Whenever the measurements are not noisy or affected by rain, both the HH and VV attenuation are observed to have a maximum at night (03:00 to 06:00) and a minimum at noon (12:00 to 16:00) and typically exhibit diurnal cycles of 1 to 1.3 dB magnitude. During rain, the attenuation at HH increases about 2.5 to 6.5 dB and at VV about 3 to 8.5 dB.

D. Diurnal Cycles in Height Layers

Diurnal cycles in the L-band reflectivity profiles over height at HH and VV were presented in a conference paper [44]. HV cycles were also investigated, but were not as significant. The analysis is, therefore, not repeated in this study. To summarize, diurnal cycles of up to more than 1 dB were seen at both HH and VV, but with completely different characteristics. The HH cycle had its minimum at night and mainly occurred in the middle canopy layers. Conversely, the VV cycle had its maximum at night and mainly occurred in the upper and lower canopy layers. Their presence over time was also different, with the HH cycle being the most apparent in May while the VV cycle was strong in June and July.

IV. Analysis of the Reflectivity Variations Through a Scattering Model

This study focuses on the presence of temporal variations in the L-band reflectivity profiles of the forest stand, as was presented in Fig. 3. In order to understand the causes of these phenomena, a scattering model is formulated, evaluated, and applied. The reflectivity profiles' temporal variations are an expression of a combination of underlying polarization-dependent scattering and extinction processes. The model described in this section connects the observed reflectivity profiles with two quantities: the vertical scattering and extinction profiles, $\sigma(z)$ and $\kappa(z)$.

A. Model of the Reflectivity Profile in Terms of Extinction and Scattering Profiles

The model is based on an incoherent single-scattering assumption for the forest canopy, where the observed reflectivity at a point in 3-D space is a function of the scattering σ (volume backscattering coefficient) of objects within the resolution cell and extinction κ along the radar LOS l. The expected reflectivity I at a point $\vec{r}$, with the radar observing from a position $\vec{r}_{\text{rad}}$, can then be expressed as

$$I(\vec{r}) = \left[\sigma(\vec{r}) e^{-2\int_{\vec{r}_{\text{rad}}}^{\vec{r}} \kappa(\vec{r}) dl}\right] * h(\vec{r}) \tag{2}$$

where $h(\vec{r})$ is the space-variant intensity point-spread function (PSF) and the asterisk denotes convolution. Note that this model assumes range spreading loss and antenna radiation pattern to have been corrected for, while neglecting atmospheric attenuation and system noise. These assumed factors and the PSF were corrected for in the radar calibration [40]. A forward model for the expected vertical reflectivity profile (VRP) measurement, with horizontal integration, is

$$\text{VRP}(z) = \iint I(x, y, z) dx dy \tag{3}$$

where y is ground range, x cross range, and z the height above ground. Inversions of (2) and (3) are ill-posed without further constraints on the spatial properties of the scattering σ and extinction κ. This is clear as an arbitrary distribution of κ can map to an arbitrary VRP for some set of σ.

To counter this problem, a number of constraints are applied to (2) in the model. First, we assume the forest canopy to consist of horizontally stratified layers, i.e., the scattering and extinction can be expressed as vertical profiles $\sigma(z)$ and $\kappa(z)$. Then, a division of the forest into two layers with different scattering properties can be motivated by the crown and trunk canopy structures, which has been adopted in previous forest scattering models [29]. The model thereby constructs scattering and extinction profiles by assuming two canopy layers with different properties. These are referred to as the "upper" and "lower" canopy layers. The model also assumes the transition between layers to contain a mix of each layer's properties according to a Gaussian function $g(s, z)$ with standard deviation parameter s. That is, with asterisk denoting convolution

$$\sigma(z) = g(s, z) * \begin{cases} 0, & z > h_u \\ \sigma_u, & h_u \geq z > h_l \\ \sigma_l, & h_l \geq z \end{cases} \tag{4}$$

and

$$\kappa(z) = g(s, z) * \begin{cases} 0, & z > h_u \\ \kappa_u, & h_u \geq z > h_l \\ \kappa_l, & h_l \geq z \end{cases} \tag{5}$$

and where subscripts u and l indicate parameters belonging to the upper and lower layers, respectively. Note that the ground backscatter is excluded in this model, since it is estimated separately in Section IV-B.

The corresponding forward model for the BorealScat radar tomography measurements is illustrated in Fig. 5. Equation (3) simplifies in this case to

$$\text{VRP}(z) = \int_{y_{\min}}^{y_{\max}} \left[\sigma(z) e^{-2sec(\theta_i(y,z)) \int_z^{\infty} \kappa(z') dz'}\right] * h'(z) dy \tag{6}$$

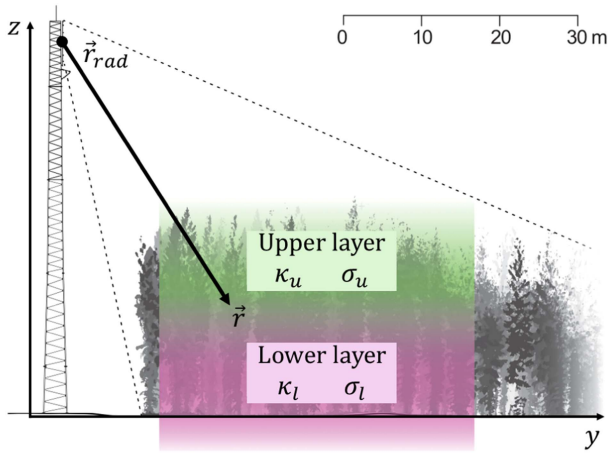

Fig. 5. BorealScat VRP measurement forward model, assuming the forest scattering and extinction to be horizontally stratified in two layers with Gaussian mixed boundaries.

where $y_{\min} = 20$ m, $y_{\max} = 70$ m, θ_i is the incidence angle, and $h'(z)$ an applied vertical smoothing function over 6 m. The exponent expresses the LOS integral of the microwave extinction down to a height z, as is seen in (2), but expressed using the extinction profile and the incidence angle. The cross-range integration in (3) is excluded in (6) since the BorealScat tower radar is beam-limited in cross-range resolution. The scattering and extinction profiles are probably also θ_i-dependent, but this was not included in the model for simplicity. However, note that this assumption concerns the scattering and extinction profiles; the model's resulting reflectivity profile still exhibits a strong incidence angle dependence due to the propagation distance in the canopy, since the model accounts for the large variation of incidence angle.

As can be noted in (4) and (5), the model for a single VRP observation is described by 7 parameters: σ_u, σ_l, κ_u, κ_l, h_u, h_l, and s. It was further assumed that only the upper layer extinction and scattering properties varied temporally, i.e., $\sigma_u(t)$ and $\kappa_u(t)$ while all other parameters are constants. This can be motivated by two arguments: the relative diurnal variations of stem radius, and thus, water content variations, are larger close to the crown than at the base [33], and it will be seen in Section IV-C that the model parameters are more sensitive in the upper than in the lower canopy.

Two constraint cases were defined for $\kappa(z,t)$. First, to correspond to the same average attenuation at the CR as observed in the two-way attenuation $L_R^2(t)$ measurements (at an incidence angle θ_R of 67°), i.e.,

$$\frac{1}{N}\sum_{i=1}^{N} e^{2\sec(\theta_R)\int_0^\infty \kappa(z,t_i)dz} = \frac{1}{N}\sum_{i=1}^{N} L_R^2(t_i). \tag{7}$$

The exponent in the leftmost term corresponds to the LOS integral of the extinction profile, in the same way as in (6), to $z = 0$ m in the ground plane where the CR is located. Note that the condition in (7) does not constraint the time variation of the model parameters. Therefore, this case is referred to as the "mean constrained" model. In the second case, the model is instead constrained by the exact time variation, which is referred to as the "time constrained" model, i.e., without the averaging in (7).

Since trihedral corner reflectors only reflect strongly at HH and VV polarizations, the HV two-way attenuation at the CR was estimated by combining the measured two-way attenuation at HH and VV as

$$L_{\mathrm{HV}}^2 = \sqrt{L_{\mathrm{HH}}^2 L_{\mathrm{VV}}^2} \tag{8}$$

and the model could thereby be evaluated for all three polarizations.

The model was fitted to the BorealScat VRP time series by minimizing the mean-squared error (MSE) between the modeled and observed VRPs over the time interval, making use of the time variation to reduce the model's solution space. MATLAB's "fmincon" function was used for solving the optimization problem. The VRPs' magnitude was normalized to its overall mean at HH. Experimentally, it was found that a good initial guess to achieve convergence was $h_u = 21$ m, $h_l = 12$ m, $s = 3$ m, $\sigma_l = 0.5$ m^2/m^2, $\kappa_l = 0.1$ dB/m, while the time-variable parameters were initiated as $\kappa_u(t) = 0.4$ dB/m and $\sigma_u(t) = 1$. Upper/lower bounds of 18/24 m, 8/16 m, 1/4 m, 0/1, 0/0.22 dB/m were used, for respective parameter. These were relatively tight bounds, found by trial-and-error, which resulted in good performance and quick convergence. The model was only fitted over the 6 to 26 m height interval, i.e., including most of the canopy reflectivity and excluding the ground response.

B. Estimation of the Ground Scattering Component

Since the canopy attenuation is measured at ground level, the model described in (6) implies that the ground backscatter can be estimated directly. That is, without the need to solve for any ill-posed inversion problem. By observing (6) for a ground scattering component $\sigma_g = \sigma(0)$ and that the extinction integral along LOS to the CR is $\int_0^\infty \kappa(z')dz' = \cos(\theta_R)L_{R,\mathrm{Np}}^2/2$, with θ_R as the incidence angle at the CR, it can be simplified to

$$\mathrm{VRP}(0) = \sigma_g h'(0)\int_{y_{\min}}^{y_{max}} e^{-\sec(\theta_i(y,0))\cos(\theta_R)ln(L_R^2)}dy. \tag{9}$$

The model assumes that σ_g is independent of the ground range y and, hence, also by the incidence angle $\theta_i(y,0)$. Also note that this assumes $\sigma_g \gg \sigma(z)|_{z\neq 0}$ within the range of z where the vertical smoothing function $h'(z)$ has an influence. Then, the ground scattering component can be solved for directly by

$$\sigma_g = \mathrm{VRP}(0)/\left(h'(0)\int_{y_{\min}}^{y_{\max}} e^{-\sec(\theta_i(y,0))\cos(\theta_R)ln(L_R^2)}dy\right). \tag{10}$$

Estimating the ground scattering σ_g is thereby a straightforward procedure.

C. Model Evaluation

Two constraint cases are evaluated in this study: one focused on validation of the model's physical relevance and one on performance of the scattering parameter estimation. For the

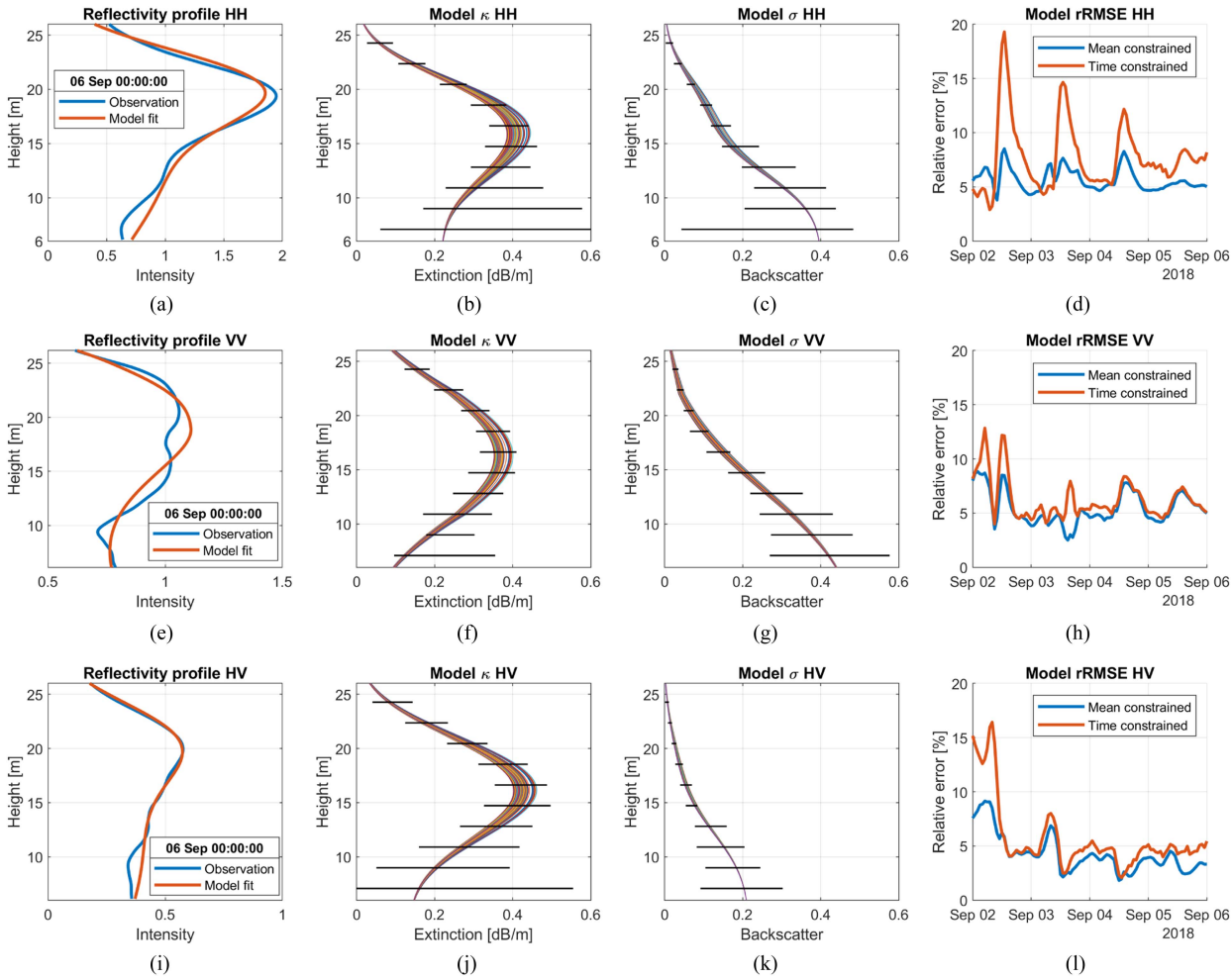

Fig. 6. Evaluation of the model, separating the L-band reflectivity profiles into extinction and scattering profiles (fitted over 6 to 26 m height). The time period spans from Sep. 2 00:00 to Sep. 6 00:00, a time window without precipitation. From left to right and for L-band HH, VV, and HV: 1) An example of the model fit to the observed reflectivity profile, 2) the model fit extinction profiles, 3) the model fit scattering profiles and 4) the model reflectivity profile rRMSE. Results for every full hour are shown in 2) and 3). The black horizontal lines indicate the sensitivity of the fit, by marking the upper and lower limits where changing a 2 m layer to this magnitude causes a 0.01 increase in rRMSE.

validation-focused "mean constrained" case, the extinction profiles were constrained to have the same average canopy attenuation as that observed in the measurements, while not constraining the time variation. This was done since the lower canopy extinction is uncertain in the model and tends to yield a large offset in total canopy attenuation. Regardless, the attenuation measurements can still be used to validate the magnitude and diurnal phase of variations in the modeled extinction for this case. For the performance-focused "time constrained" case, the model is further constrained to exactly follow the time variation of the measured canopy attenuation. This reduces the model's solution space, which is expected to improve the parameter estimation, but then the attenuation measurements cannot be used for validation.

An evaluation of the model fit is shown in Fig. 6, for 4 days in the beginning of September. This was the longest precipitation-free time window in the later growth season, where the canopy attenuation measurements were of good quality at both HH and VV. The model was fitted over the 6 to 26 m height interval. The plots in column 1 compares the modeled and the observed reflectivity profile in September 6 at midnight, at HH, VV, and HV in respective row. Columns 2 and 3 show the corresponding model extinction and scattering profiles, $\kappa(z)$ and $\sigma(z)$, at every full hour during the four-day time period. The black horizontal lines indicate the sensitivity of the model fit to the magnitude in the profiles. They mark the upper and lower limits where changing the magnitude in a 2 m height layer to this level causes a 0.01 increase in relative RMSE (rRMSE), i.e., error ratio to the mean intensity of the observed reflectivity profile. Column 4 shows the model rRMSE over the four-day period for the "mean constrained" and "time constrained" cases. Columns 1 to 3 were obtained using the "time constrained" model.

The model-estimated extinction and scattering profiles in columns 2 and 3 of Fig. 6 are similar between the polarizations, despite that the observed reflectivity profiles' peak intensity and dynamic range is about a factor 2 higher at HH compared to VV, as can be seen in column 1. The extinction is strongest in the upper canopy, with a peak value of about 0.4 dB/m, and the

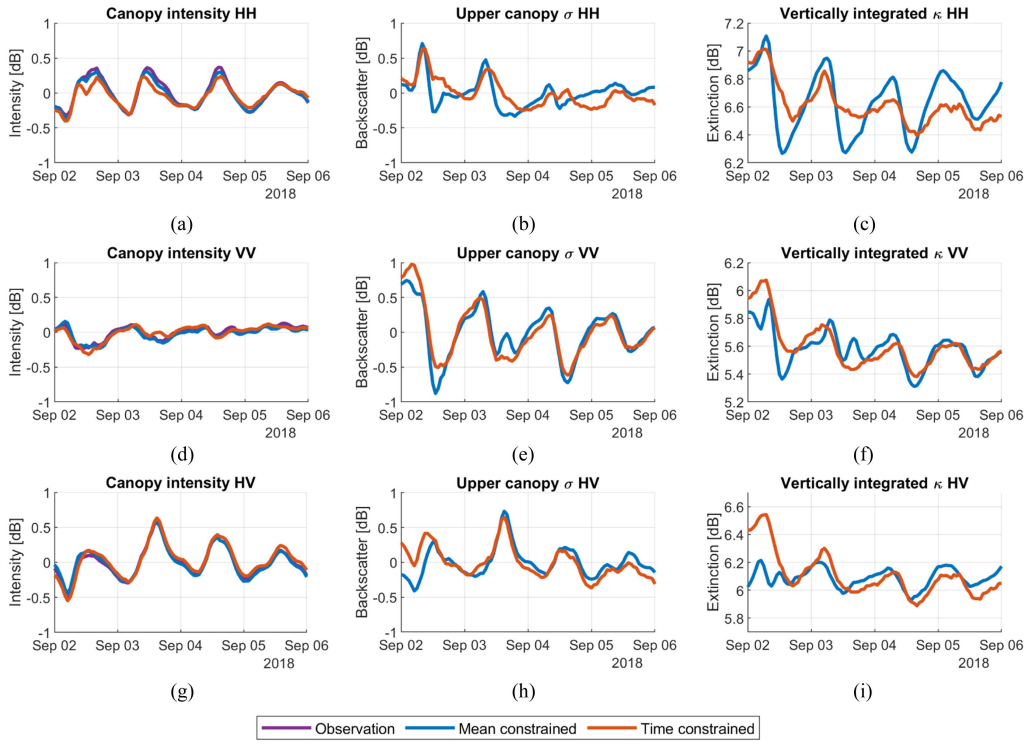

Fig. 7. Time series of canopy intensity and vertically integrated extinction and scattering, as obtained from the model-estimated parameters.

scattering is largest in the lower canopy, crossing half of its peak value at about 15 m height. The variation of the profiles over time is small, at most about $\pm 7\%$ (0.5 dB) around the mean over time. Apart from the HV scattering profile having a magnitude half of that at HH and VV, only small differences are observed. It is apparent from the black $\pm 1\%$ rRMSE lines that the upper canopy extinction and especially scattering has the largest impact on the overall shape of the modeled reflectivity profile.

The model manages to fit the observations with often less than 10% and down to about 5% error, as can be seen in the model fit examples in column 1 and the rRMSE plots of column 4. The time-constrained case shows larger deviations from the mean-constrained case at HH and HV than at VV, indicating that the model fits better at VV.

The time variation of the model-estimated extinction and scattering parameters is evaluated in Fig. 7 for the mean and time constrained cases. The plots in column 1 compares the corresponding canopy intensity of the modeled reflectivity profiles with that observed. The models follow the observations closely at each polarization.

Column 2 of Fig. 7 shows the time-variation of the upper canopy scattering parameter σ_u. Notably, strong diurnal cycles are present at VV with a magnitude about 1 dB, despite that no such are seen in the canopy intensity. The cycles have a maximum at night and early morning, corresponding to expected stem water content changes in the trees. The canopy scattering at HH and HV tends to exhibit a maximum around noon.

The model-estimated extinction's temporal variation is evaluated in column 3 of Fig. 7 by comparing the vertically integrated extinction for the two model constraint cases. The time constrained case simply shows the extinction integral inferred directly by the measured canopy attenuation. This serves as a validation of the mean constrained case's estimated extinction. The mean constrained model performs well, considering the complexity of forest scattering processes. The agreement is not perfect, as the HH estimated extinction overshoots that measured by twice the magnitude (in dB), there is a deviating peak in the VV extinction at Sep. 3 at noon and the extinction at HV differs significantly in Sep 2. Apart from these discrepancies, the diurnal phase of the variations all agree and the extinction at VV and HV closely resembles that measured.

The agreement between the mean and time constrained models verifies the model's applicability. That is, the model is able to estimate a canopy attenuation variation similar to that measured at the CR, validating the model-estimated extinction parameter. In addition, constraining the time variation of the extinction yields a similar but cleaner variation in canopy scattering, supporting the meaningfulness of the estimated canopy scattering variations at VV and HV. The estimated HH scattering remains more uncertain, as the larger error peaks at HH in Fig. 6, column 4, indicates degraded performance. The quality of the VV scattering parameter is likely better for the time constrained than for the mean constrained model, and the former is applied for the remaining analysis.

D. Model-Estimated Upper Canopy Scattering Variations During the Drought Period

The time-constrained model was applied to study the model-estimated upper canopy scattering variation during the drought period, as shown in Fig. 8. The observed canopy intensity

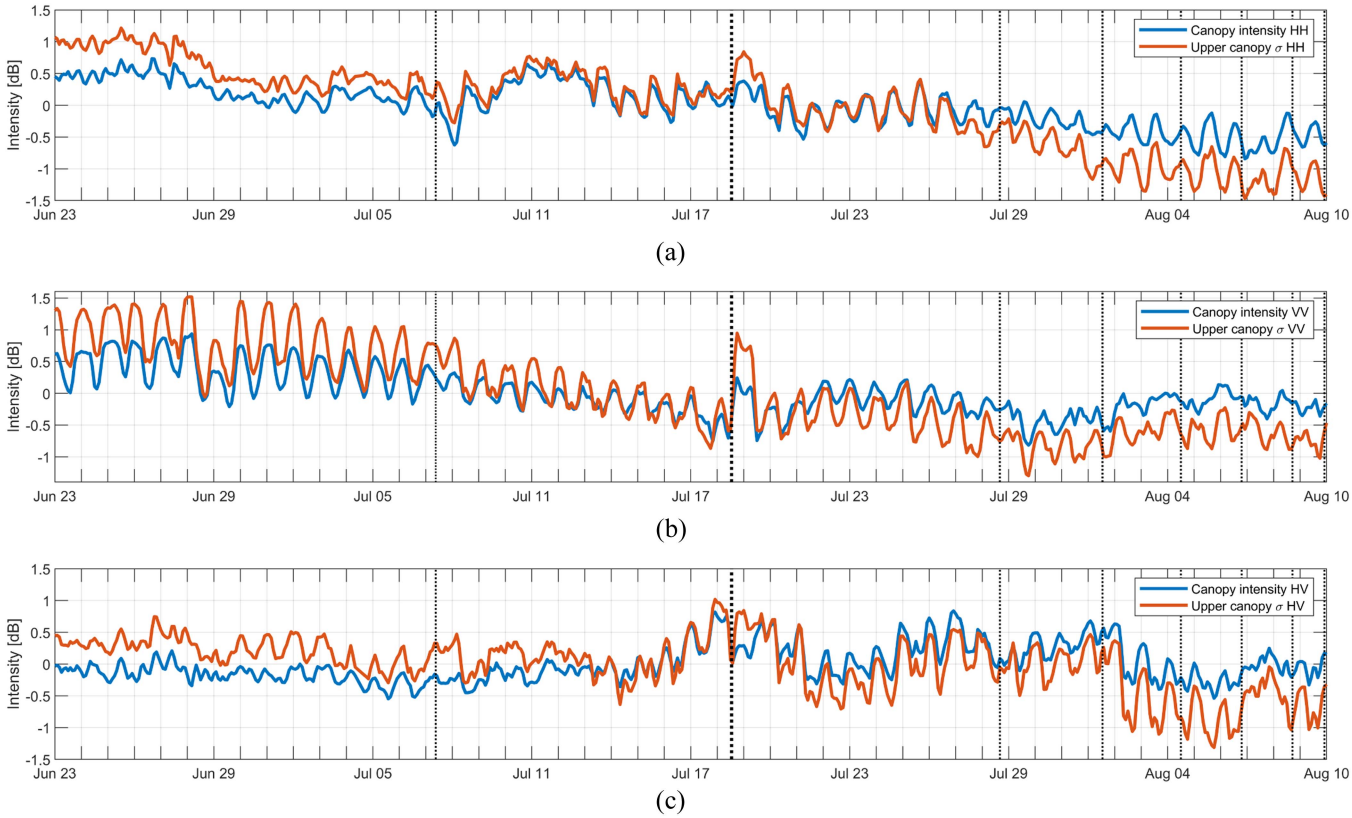

Fig. 8. Time series of L-band canopy intensity and model-estimated upper canopy scattering σ_u variations during the drought period in 2018. The vertical black dotted lines mark the few rain events, with a thicker line for the slightly more intense rain event in July 18. The time-axis ticks mark midnight. Note how the diurnal cycles in the VV canopy intensity disappear by August, while they still are present in the VV canopy scattering.

variation is also included for comparison. Over this long time period the mean-constrained model was not able to estimate an extinction variation corresponding to the canopy attenuation variation, missing the decrease over time. In addition, the estimated scattering is both of highest quality and interest at VV, since the VV attenuation measurements were good enough to discern diurnal variations over the time period, which was not the case at HH (see Fig. 4); and the VV scattering in Fig. 7 appears directly related to expected stem water content variations, i.e., it shows a maximum at night.

In Fig. 8, note the similarity between the model-estimated canopy scattering and the observed intensity in terms of diurnal variations and the successive decrease during the time period. At HH, diurnal cycles with a maximum at noon appears as the drought progresses. At VV, both quantities exhibit clear diurnal cycles with a maximum at night, which drop in magnitude over time, and an intensity peak during the brief rain event on July 18; the main difference lie in the magnitude of the variations, which are more pronounced for the scattering, and while the intensity no longer exhibits any diurnal cycles by the beginning of August, the scattering still does. At HV, diurnal cycles appear with a maximum at night, especially in the later half of the drought, and are more strongly expressed in the scattering. A common trait between all polarizations is that the scattering decreases more throughout the drought than the observed intensity, especially in the weeks toward the end.

V. Correlations With Environmental Parameters

In this section, the radar quantities' dependencies on SM and VPD are analyzed over the growth season and with focus on the drought period. The radar quantities include the canopy intensity I_c and the ground intensity I_g, as were described in Section III and seen in Fig. 4. Also included is the two-way attenuation L^2 measured at the CR, where the corresponding HV attenuation is estimated from the HH and VV attenuation by (8). Two model-estimated radar scattering quantities are analyzed: the canopy scattering σ_u, as provided by the model in Section IV-D, and the ground scattering σ_g, obtained through (10).

The physical causes of the reflectivity changes in the forest are likely a combination of different biophysiological processes, acting with either mostly subdaily dynamics (tree sap flow, stem water content, temperature) or more long-term dynamics (SM, tree water stress, mean temperature). Therefore, two temporal components of the quantities are studied independently: the diurnal variations and the daily averages.

A. Correlations for Diurnal Variations

The diurnal variations of the canopy-related radar quantities were obtained by normalizing their magnitudes to the daily average, i.e., the mean over 24 h centered around each sample point. Correlation plots with VPD over the drought period are compiled in Fig. 9. Data ± 12 h around detected precipitation are

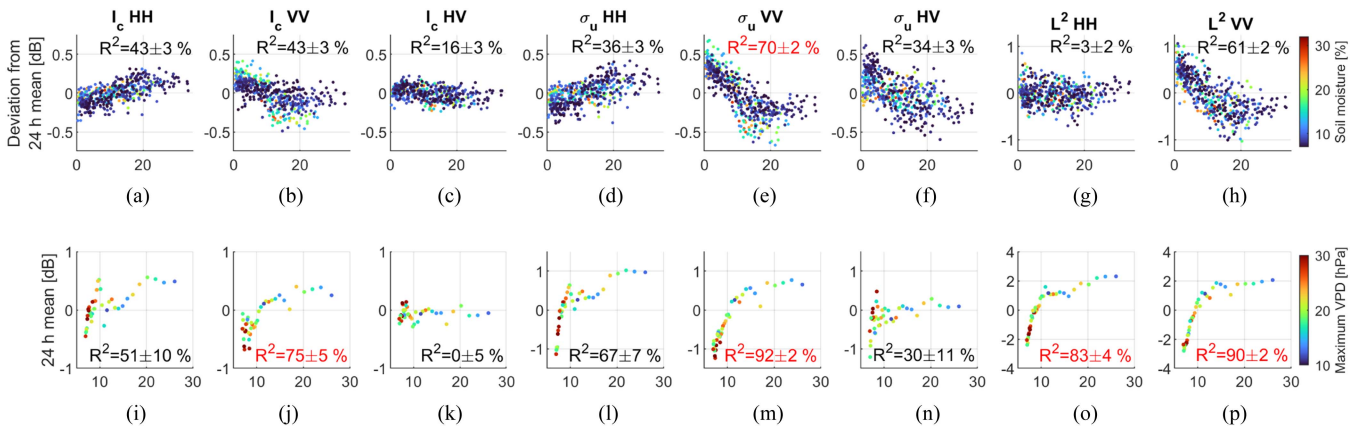

Fig. 9. Correlation plots with VPD and SM during the drought period, spanning from June 23 to August 10. The analyzed quantities are the canopy intensity I_c, the model-estimated upper canopy scattering σ_u and the two-way attenuation L^2 at the CR. The R^2-values were obtained by a quadratic fit. Row 1: Samples were obtained at every full 2 h (477 in total and with precipitation excluded) and are normalized to their daily average, i.e., the 24 h mean around each sample. Row 2: Samples were obtained every midnight (40 in total and with precipitation excluded) and are the daily averages.

excluded. The coefficient of determination R^2, as obtained by a quadratic fit (which is able to account for the intensity saturation), is included in the plots. Its confidence interval is given as its standard deviation; this was estimated from the RMSE of the fit, assuming the residuals to be zero-mean Gaussian distributed and by simulating a large number of measurements.

In general, all the VV quantities show a decrease with increasing VPD and a saturation phenomena for VPD values above about 20 hPa. This is probably an effect of stomatal closure limiting stem water depletion, as it was observed in [34] to be initiated in *P. abies* by a VPD of 15 hPa. Conversely, the HH canopy intensity and scattering show an increase with VPD and any corresponding saturation phenomena is not discernible. At HV, the intensity shows no correlation with VPD, while the scattering resembles a similar, albeit weaker, correlation as that at VV, decreasing with VPD. The span (magnitude of variation) of the VV canopy intensity's and scattering's VPD dependence decreases as SM delves below 10%. Meanwhile, the span of the canopy attenuation's diurnal variation remains the same throughout the drought period.

A notable result is that the model-estimated canopy scattering shows significantly stronger correlation with VPD than any of the other quantities. Compare its R^2 of 0.70 with the VV canopy intensity R^2 of 0.43. These results support the hypothesis that the observed intensity is affected by a mix of extinction and scattering mechanisms, obscuring dependencies on forest water dynamics.

B. Correlations for Daily Averages

Fig. 9, Row 2, shows the canopy-related radar quantities' daily averages' correlation with SM, for samples taken every day at midnight (excluding precipitation) during the drought period. Just as for Row 1 in the figure, the R^2 values were obtained by a quadratic fit. In general, except for the HV intensity, the quantities decrease as SM decreases. The HH canopy intensity shows a more complex dependence, while that at HV is completely uncorrelated with SM.

It is apparent that the canopy scattering exhibits a more clear dependence on SM than the canopy intensity. Compare the excellent $R^2_{\sigma_u,\mathrm{VV}} = 0.92$ with $R^2_{Ic,\mathrm{VV}} = 0.75$, which still implies a strong correlation for the VV canopy intensity with SM. Also note the 2 dB span of the daily average canopy scattering, while that is only about 1 dB for the VV canopy intensity. The main difference lies in the dependence for low SM levels, where the variance of the canopy intensity increases significantly while the canopy scattering continues to decrease within a precise trajectory.

The daily average attenuation also shows an excellent correlation with the SM decrease during the drought, where $R^2_{L^2,\mathrm{VV}} = 0.90$. The reduction in VV canopy intensity and scattering, as well as attenuation, with decreasing SM is an effect that can be expected due to the low SM levels causing tree water stress. Note how the daily averages of the radar quantities in Fig. 9 are considerably stable for SM levels above about 15%. Although, a sudden drop in VV I_c, σ_u, and L^2 was seen during a day of about 17% SM. This occurred during two days of high maximum VPD, whereafter the quantities "recovered" during a day of low maximum VPD.

Finally, lets focus on what the radar observes below the forest canopy: the ground intensity and scattering. The daily averages' correlation with SM are shown in Fig. 10, also including the canopy attenuation as it was used to estimate the ground scattering. The time period ranges from June 1 to October 1, including all precipitation events. The quantities were delayed by 10 h, which was observed to best align them with the changes in SM. Such a delay can be explained by a time required for precipitated water to distribute throughout the soil around the SM sensor's location under the forest canopy.

Note the significantly higher R^2 (obtained using a linear fit) for the ground scattering compared to that of the ground intensity, especially at HV and VV. Although, the HH attenuation measurements were more noisy, which may affect the ground scattering estimation. Temporal variation of backscatter from a rough soil surface at L-band is expected to depend primarily on SM, since the surface rms height and correlation length are

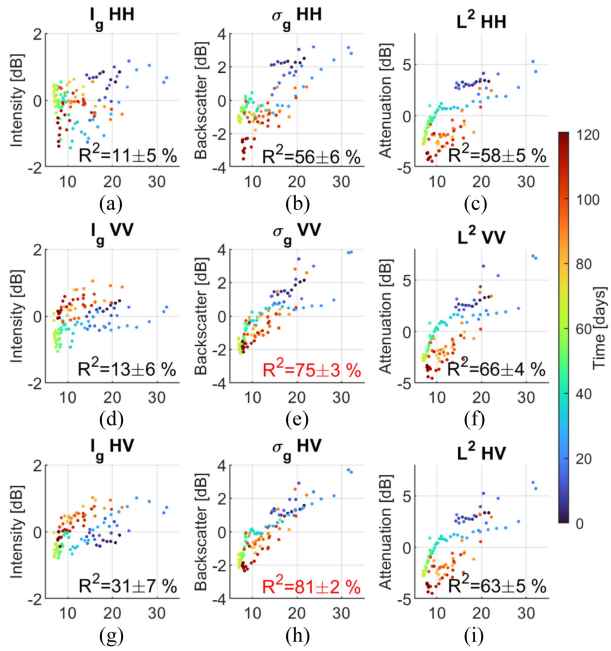

Fig. 10. Correlation plots with SM from June 1 to October 1, with a sample every midnight (precipitation included). Each sample (115 in total) is the average over a day. The analyzed quantities are the ground intensity I_g, model-estimated ground backscatter σ_g and two-way attenuation L^2 at the CR. A delay of 10h was introduced on the quantities, to align them with the variation in SM. The R^2 values were obtained by a linear fit.

likely to be constant. The SM dependence of backscatter in dB from bare soil at L-band can be close to linear [45], [46]. The presence of a forest on top of the soil surface adds scattering components that map to the ground height [30]. Such scattering components are typically stronger at HH and VV than at HV, which could explain a more direct SM dependence at HV.

VI. Discussion

A model was formulated for the purpose of understanding the interplay of scattering and extinction mechanisms in the forest reflectivity, to reveal underlying connections to its water dynamics. This model is essentially representing an attenuating layer containing scatterers, with a distribution over height and with dielectric properties varying over time. One could apply microwave scattering models, such as MIMICS and MIPERS to simulate the radar observations over the forest stand [29], [47], but that requires detailed structural and dielectric information of the forest, on a level not available for the BorealScat forest stand. Thereby the need to formulate a specific model for the BorealScat measurements, relying solely on single-polarization radar observables. Furthermore, provided an accurate EM simulation, the formulated model's vertical distributions $\kappa(z)$ and $\sigma(z)$ could be computed and used to evaluate the model.

While the formulated model captures the strong incidence angle dependence of the reflectivity that comes from signal propagation distance through the canopy, there should also be incidence angle dependencies in its components. The formulated model assumes no such dependencies, and this assumption's consequences for the analysis should be assessed. Importantly, the extinction (i.e., attenuation per distance) at L-band is supposedly weakly incidence angle dependent, as GNSS-VOD measurements (VOD is proportional to extinction) were observed constant over elevation [48], and the same was indicated in SAR campaigns observing trihedral corner reflectors in forests [49], [50]. Although, some dependence is evident by the observed absolute differences in HH and VV canopy attenuation in this study, and differences between forest types are expected. However, given weakly dependent extinction, the main errors map to the absolute magnitudes of the model-estimated scattering parameters (which are incidence angle dependent). This is a minor concern for our results since we are studying their relative temporal variations, while the observation geometry remains fixed. Modeling of further incidence angle dependence would also add significantly to the model's complexity as well as require assumptions about the forest's structural properties.

Physical parameters of interest are the forest evapotranspiration and tree water stress status, as is indicated by the VPD and SM measurements. It is of course sought for to model the forest reflectivity in terms of these parameters, to enable estimation of them by inversion from radar measurements. However, the understanding of relations between radar measurements and forest water dynamics is currently in embryo. The correlation analysis results in this article highlight these connections, pinpointing the importance of interacting extinction and scattering components in temporal variations of forest reflectivity at L-band, adding to an active field of research.

Obtaining a complete understanding of the relationships between forest water dynamics and radar observations will require the following:

1) detailed monitoring and modeling of the water transport in trees, forest undergrowth and soil;
2) accurate electromagnetic modeling of the forest from structural and dielectric properties;
3) even more precise radar measurements.

With this purpose in mind, the BorealScat-2 tower radar experiment has been developed and is currently collecting data [51], [52].

Finally, we should mention a few unaccounted factors in this study. Most apparently, there are inaccuracies in the VPD estimation and its connections to transpiration; The SVP estimate in (1) is an approximation, and the transpiration is also further driven by wind and solar irradiance. In addition, the dependence on temperature of the trees' dielectric constant and the microwave extinction at L-band between 10 to 30 °C may be non-negligible when compared to those of diurnal water content variations [48], [53], [54]. The studies report on different and uncertain dependencies on temperature, with some decreasing, some increasing, and some being constant. In the extremes, such dependencies may be comparable to those of diurnal water content variations. Connections to temperature were examined, by repeating the analysis in Fig. 9 for temperature, but this was excluded due to all such being weaker than those observed for VPD (which in itself is strongly dependent on temperature) and SM.

VII. Conclusion

This study has presented and analyzed time series of L-band reflectivity and attenuation observed by the BorealScat multipolarization tomographic radar in a *P. abies* stand. We focus on a time period where the forest stand was exposed to drought and, hence, experienced water stress, triggering an *Ips typographus* infestation that led to tree deaths in the following years.

It was found that the canopy intensity I_c (reflectivity above 4 m height) exhibited diurnal cycle phenomena, which presence over time varied, also between polarizations, where the temporal changes were mostly opposite between HH and VV. In addition, the two-way attenuation L^2 showed covarying diurnal cycles between HH and VV with a maximum at night. The absolute attenuation dropped significantly during the period of drought, and was generally larger at HH than at VV.

These unique observations, with surprising temporal and polarization differences, are clearly an expression of underlying interacting microwave scattering mechanisms. To bring understanding to these phenomena, a model was formulated; it expresses the reflectivity profile in terms of microwave scattering and extinction profiles, estimating two time-variable parameters: the upper canopy scattering σ_u and extinction κ_u.

Model-estimated σ_u over the drought period was compared with I_c, and σ_u showed a larger drop in intensity during the drought, as well as stronger and more consistent diurnal cycles. Notably, at VV, σ_u exhibited strong diurnal variations of up to 1.5 dB with a maximum at night, i.e., characteristics expected from stem water content variations, even at times when there were no apparent variations in I_c. This was also a trend at HV, while quantities at HH consistently expressed diurnal cycles with a maximum at noon, indicating that the HH diurnal variations may be driven mainly by microwave extinction.

A main result is that the model-estimated scattering σ_u was more strongly connected to forest water dynamics than any other quantity, with similar connections seen for L^2. This was concluded from correlations of diurnal variations with VPD, indicating sensitivity to transpiration activity, and correlations of daily averages with SM, indicating a dependence on tree water stress. Notably, there was a saturation effect in VV I_c, σ_u, and L^2, for days with high VPD, consistent with stomatal closure limiting stem water depletion. Finally, model-estimation of the ground scattering σ_g showed a significant increase in the correlation with SM (also including precipitation) compared to that of the ground intensity I_g (reflectivity below 4 m height).

To summarize, the unique contributions of this study are as follows:

1) the multipolarimetric L-band forest reflectivity profile and attenuation time series measurements;
2) that temporal phenomena can be explained by interacting mechanisms between microwave extinction and scattering;
3) that these mechanisms may be decomposed by model-based estimation;
4) that this produces more direct relations to forest transpiration, water stress, and SM.

Our results show that spaceborne L-band SAR missions aimed at using diurnal variations in forest reflectivity for monitoring forest water status, such as the proposed SLAINTE mission [22], need to account for the interacting microwave scattering and extinction mechanisms in the forest reflectivity. The results also show that the sensitivity of L-band SAR to tree water stress and SM in forests can be significantly improved by accounting for these mechanisms. Furthermore, spaceborne SAR needs to correct for Faraday rotation since the diurnal signatures are polarization-dependent [55].

Acknowledgment

The authors would like to thank Skogsstyrelsen for data on tree death and damage caused by *Ips typographus* in the forest stand observed by the BorealScat tower radar.

References

[1] S. Trumbore, P. Brando, and H. Hartmann, "Forest health and global change," *Science*, vol. 349, pp. 814–818, 2015.
[2] F. Lloret and E. Batllori, "Climate-induced global forest shifts due to heatwave-drought," in *Ecosystem Collapse and Climate Change*. New York, NY, USA: Springer, 2021, pp. 155–186.
[3] H. Hartmann et al., "Climate change risks to global forest health: Emergence of unexpected events of elevated tree mortality worldwide," *Annu. Rev. Plant Biol.*, vol. 73, pp. 673–702, 2022.
[4] S. Gauthier, P. Bernier, T. Kuuluvainen, A. Z. Shvidenko, and D. G. Schepaschenko, "Boreal forest health and global change," *Science*, vol. 349, pp. 819–822, 2015.
[5] G. B. Bonan, "Forests and climate change: Forcings, feedbacks, and the climate benefits of forests," *Science*, vol. 320, pp. 1444–1449, 2008.
[6] S. C. Steele-Dunne, J. Friesen, and N. van de Giesen, "Using diurnal variation in backscatter to detect vegetation water stress," *IEEE Trans. Geosci. Remote Sens.*, vol. 50, no. 7, pp. 2618–2629, Jul. 2012.
[7] A. G. Konings, Y. Yu, L. Xu, Y. Yang, D. S. Schimel, and S. S. Saatchi, "Active microwave observations of diurnal and seasonal variations of canopy water content across the humid African tropical forests," *Geophys. Res. Lett.*, vol. 44, pp. 2290–2299, 2017.
[8] T. van Emmerik et al., "Water stress detection in the Amazon using radar," *Geophys. Res. Lett.*, vol. 44, pp. 6841–6849, 2017.
[9] L. M. H. Ulander, A. R. Monteith, M. J. Soja, and L. E. B. Eriksson, "Multiport vector network analyzer radar for tomographic forest scattering measurements," *IEEE Geosci. Remote Sens. Lett.*, vol. 15, no. 12, pp. 1897–1901, Dec. 2018.
[10] A. R. Monteith and L. M. H. Ulander, "Temporal survey of P- and L-band polarimetric backscatter in boreal forests," *IEEE J. Sel. Topics Appl. Earth Observ. Remote Sens.*, vol. 11, no. 10, pp. 3564–3577, Oct. 2018.
[11] A. R. Monteith and L. M. H. Ulander, "Temporal characteristics of P-band tomographic radar backscatter of a boreal forest," *IEEE J. Sel. Topics Appl. Earth Observ. Remote Sens.*, vol. 14, pp. 1967–1984, 2021.
[12] F. Ulaby et al., *Microwave Radar and Radiometric Remote Sensing*. Ann Arbor, MI, USA: Univ. of Michigan Press, 2014.
[13] A. Sellin, "Hydraulic and stomatal adjustment of Norway spruce trees to environmental stress," *Tree Physiol.*, vol. 21, pp. 879–888, Aug. 2001.
[14] A. Hamadi et al., "Temporal survey of polarimetric P-band scattering of tropical forests," *IEEE Trans. Geosci. Remote Sens.*, vol. 52, no. 8, pp. 4539–4547, Aug. 2014.
[15] S. Netherer et al., "Drought increases Norway spruce susceptibility to the Eurasian spruce bark beetle and its associated fungi," *New Phytologist*, vol. 242, pp. 1000–1017, 2024.
[16] M. Palomeque, J. Ferreyra, and M. Thibeault, "Monitoring results of the SAOCOM-1 constellation: A mission overview and summary of results," *IEEE Geosci. Remote Sens. Mag.*, vol. 13, no. 2, pp. 49–57, Jun. 2025.
[17] M. Ohki, T. Motohka, Y. Kankaku, S. H. Miura, T. Tadono, and Y. Arikawa, "Advanced land observing satellite-4: Mission concepts and technical overview: Pioneering a new era of L-band SAR," *IEEE Geosci. Remote Sens. Mag.*, vol. 13, no. 2, pp. 35–40, Jun. 2025.
[18] T. Li, X. Tang, X. Zhang, J. Lu, and X. Zhang, "Current status and prospects of the LuTan-1 mission," in *Proc. IEEE Int. Conf. Signal, Inf. Data Process.*, 2024, pp. 1–4.

[19] P. A. Rosen et al., "The NASA-ISRO SAR mission: A summary," *IEEE Geosci. Remote Sens. Mag.*, vol. 13, no. 2, pp. 8–34, Jun. 2025.
[20] M. W. J. Davidson and R. Furnell, "ROSE-L: Copernicus L-band SAR mission," in *Proc. IEEE Int. Geosci. Remote Sens. Symp.*, 2021, pp. 872–873.
[21] K. Scipal and M. Davidson, "The SAOCOM-CS mission: ESA's first bistatic and tomographic L-band mission," in *Proc. IEEE Int. Geosci. Remote Sens. Symp.*, Fort Worth, TX, USA, 2017, pp. 123–124.
[22] S. Steele-Dunne et al., "SLAINTE: A sub-daily (In)SAR mission idea to study vegetation water, health and carbon," in *Proc. EGU Gen. Assem.*, Vienna, Austria, 2024, Paper EGU24-17362.
[23] C. Albinet et al., "TropiSCAT: A ground based polarimetric scatterometer experiment in tropical forests," *IEEE J. Sel. Topics Appl. Earth Observ. Remote Sens.*, vol. 5, no. 3, pp. 1060–1066, Jun. 2012.
[24] D. H. T. Minh et al., "Vertical structure of P-band temporal decorrelation at the paracou forest: Results from TropiScat," *IEEE Geosci. Remote Sens. Lett.*, vol. 11, no. 8, pp. 1438–1442, Aug. 2014.
[25] S. E. I. Essebtey, L. Villard, P. Borderies, T. Koleck, B. Burban, and T. L. Toan, "Long-term trends of P-band temporal decorrelation over a tropical dense forest-experimental results for the BIOMASS mission," *IEEE Trans. Geosci. Remote Sens.*, vol. 60, 2022, Art. no. 5102415.
[26] S. E. I. Essebtey et al., "Temporal decorrelation of tropical dense forest at C-band: First insights from the TropiScat-2 experiment," *IEEE Geosci. Remote Sens. Lett.*, vol. 17, no. 6, pp. 928–932, Jun. 2020.
[27] C. Albinet et al., "First results of AfriScat, A tower-based radar experiment in African forest," in *Proc. IEEE Int. Geosci. Remote Sens. Symp.*, Milan, Italy, 2015, pp. 5356–5358.
[28] J. J. Ruiz et al., "SodSAR: A tower-based 1–10 GHz SAR system for snow, soil and vegetation studies," *Sensors*, vol. 20, 2020, Art. no. 6702.
[29] P. Liang, M. Moghaddam, L. Pierce, and R. Lucas, "Radar backscattering model for multilayer mixed-species forests," *IEEE Trans. Geosci. Remote Sens.*, vol. 43, no. 11, pp. 2612–2626, Nov. 2005.
[30] F. T. Ulaby, K. Sarabandi, K. McDonald, M. Whitt, and M. C. Dobson, "Michigan microwave canopy scattering model," *Int. J. Remote Sens.*, vol. 11, pp. 1223–1253, 1990.
[31] S. Tebaldini, D. H. T. Minh, M. M. d'Alessandro, L. Villard, T. L. Toan, and J. Chave, "The status of technologies to measure forest biomass and structural properties: State of the art in SAR tomography of tropical forests," *Surveys Geophys.*, vol. 40, pp. 779–801, 2019.
[32] K. McDonald, R. Zimmermann, and J. Kimball, "Diurnal and spatial variation of xylem dielectric constant in Norway Spruce (Picea abies [L.] Karst.) as related to microclimate, xylem sap flow, and xylem chemistry," *IEEE Trans. Geosci. Remote Sens.*, vol. 40, no. 9, pp. 2063–2082, Sep. 2002.
[33] I. Offenthaler, P. Hietz, and H. Richter, "Wood diameter indicates diurnal and long-term patterns of xylem water potential in Norway spruce," *Trees - Struct. Function*, vol. 15, pp. 215–221, 2001.
[34] R. Zweifel, J. P. Bohm, and R. Hasler, "Midday stomatal closure in Norway spruce–reactions in the upper and lower crown," *Tree Physiol.*, vol. 22, pp. 1125–1136, 2002.
[35] T. Leistner, A. R. Monteith, J. G. Lopez, and L. M. H. Ulander, "Estimating stem water content from tower-based L-band tomographic radar using a single-scattering model of a uniform layer: A first in situ experiment," *IEEE J. Sel. Topics Appl. Earth Observ. Remote Sens.*, vol. 19, pp. 3477–3487, 2026.
[36] S. Razafindratsima, Z. M. Sbartaï, and F. Demontoux, "Permittivity measurement of wood material over a wide range of moisture content," *Wood Sci. Technol.*, vol. 51, pp. 1421–1431, 2017.
[37] L. M. H. Ulander, A. Gustavsson, B. Flood, P. Dubois-Fernandez, X. Debuis, and J. Holmgren, "BioSAR 2010 technical assistance for the development of airborne SAR and geophysical measurements during the BioSAR 2010 experiment," European Space Agency, Paris, France, Tech. Rep. 4000102285/10/NL/JA/ef, 2011.
[38] H. Petersson, "Biomassafunktioner för trädfaktorer av tall, gran och björk i sverige," Swedish University of Agricultural Sciences, Uppsala, Sweden, Tech. Rep. Arbetsrapport 59, 1999.
[39] N. Gyllenstrand, D. Clapham, T. Källman, and U. Lagercrantz, "A Norway spruce FLOWERING LOCUS T homolog is implicated in control of growth rhythm in conifers," *Plant Physiol.*, vol. 144, pp. 248–257, 2007.
[40] A. R. Monteith, L. M. Ulander, and S. Tebaldini, "Calibration of a ground-based array radar for tomographic imaging of natural media," *Remote Sens.*, vol. 11, 2019, Art. no. 2924.
[41] L. M. H. Ulander, A. R. Monteith, and M. Rönnfalk, "BorealScat - technical assistance for the deployment of a tower-based radar and geophysical measurements during the BorealScat experiment," European Space Agency (ESA), Paris, France, Tech. Rep. 4000118576/16/NL/FF/mg, 2023.
[42] A. R. Monteith and L. M. H. Ulander, "A tower-based radar study of temporal coherence of a boreal forest at P-, L-, and C-bands and linear cross polarization," *IEEE Trans. Geosci. Remote Sens.*, vol. 60, 2022, Art. no. 4402315.
[43] O. A. Alduchov and R. E. Eskridge, "Improved magnus form approximation of saturation vapor pressure," *J. Appl. Meteorol.*, vol. 35, pp. 601–609, 1996.
[44] P. J. Bennet, A. R. Monteith, and L. M. H. Ulander, "Diurnal cycles of L-band tomographic SAR backscatter in a boreal forest during summer: Observations by the BorealScat tower radar," in *Proc. IEEE Int. Geosci. Remote Sens. Symp.*, Pasadena, CA, USA, 2023, pp. 2195–2198.
[45] F. T. Ulaby, P. P. Batlivala, and M. C. Dobson, "Microwave backscatter dependence on surface roughness, soil moisture, and soil texture: Part I—Bare soil," *IEEE Trans. Geosci. Electron.*, vol. GE-16, no. 4, pp. 286–295, Oct. 1978.
[46] F. Capodici, A. Maltese, G. Ciraolo, G. L. Loggia, and G. D'Urso, "Coupling two radar backscattering models to assess soil roughness and surface water content at farm scale," *Hydrological Sci. J.*, vol. 58, pp. 1677–1689, 2013.
[47] M. A. Tanase et al., "Synthetic aperture radar sensitivity to forest changes: A simulations-based study for the Romanian forests," *Sci. Total Environ.*, vol. 689, pp. 1104–1114, 2019.
[48] V. Humphrey and C. Frankenberg, "Continuous ground monitoring of vegetation optical depth and water content with GPS signals," *Biogeosciences*, vol. 20, pp. 1789–1811, 2023.
[49] J. G. Fleischman, S. Ayasli, E. M. Adams, and D. R. Gosselin, "Foliage attenuation and backscatter analysis of SAR imagery," *IEEE Trans. Aerosp. Electron. Syst.*, vol. 32, no. 1, pp. 135–144, Jan. 1996.
[50] L. A. Bessette and S. Ayasli, "Ultra-wideband P-3 and CARABAS II foliage attenuation and backscatter analysis," in *Proc. IEEE Radar Conf.*, 2001, pp. 357–362.
[51] L. M. H. Ulander, A. R. Monteith, H. J. Persson, and J. E. S. Fransson, "Borealscat-2: Backscatter measurements of forest water dynamics," in *Proc. IEEE Int. Geosci. Remote Sens. Symp.*, Athens, Greece, 2024, pp. 2332–2335.
[52] A. Monteith et al., "A tower-based radar experiment for studying the effects of boreal forest tree-water relations," *Remote Sens. Environ.*, pp. 1–31, 2024, doi: 10.2139/ssrn.4991471. [Online]. Available: https://www.ssrn.com/abstract=4991471
[53] M. Schwank et al., "Temperature effects on L-band vegetation optical depth of a boreal forest," *Remote Sens. Environ.*, vol. 263, 2021, Art. no. 112542.
[54] A. N. Romanov, "Some behavior features of dielectric properties of water in birch wood at a frequency of 1.41 GHz," *IEEE Trans. Geosci. Remote Sens.*, vol. 60, 2022, Art. no. 4409208.
[55] F. J. Meyer and J. B. Nicoll, "Prediction, detection, and correction of Faraday rotation in full-polarimetric L-band SAR data," *IEEE Trans. Geosci. Remote Sens.*, vol. 46, no. 10, pp. 3076–3086, Oct. 2008.

Patrik J. Bennet received the B.Sc. degree in electrical engineering and the M.Sc. degree in communication engineering from the Chalmers University of Technology, Gothenburg, Sweden, where he has been working toward the Ph.D. degree in radio and space science since May 2021.

His research focuses on radar remote sensing of forests, with an emphasis on radar tomography for biomass estimation and the temporal characteristics related to forest water dynamics.

Albert R. Monteith received the M.Sc. degree in electrical engineering and the Ph.D. degree in radio and space science from the Chalmers University of Technology, Gothenburg, Sweden, in 2015 and 2020, respectively.

He is currently a Research Specialist with the Department of Space, Earth and Environment. His research interests include temporal aspects of radar remote sensing of forests, the development of multi-channel imaging radars and new radar applications at millimetre and submillimetre wavelengths.

Lars M. H. Ulander (Fellow, IEEE) received the M.Sc. degree in engineering physics and the Ph.D. degree in electrical and computer engineering from the Chalmers University of Technology, Gothenburg, Sweden, in 1985 and 1991, respectively.

Since 2014, he has been a Professor in Radar Remote Sensing with the Chalmers University of Technology. He also holds a part-time role with the Swedish Defence Research Agency (FOI), Linköping, Sweden. He is author or coauthor of more than 400 professional publications, of which more than 80 are in peer-reviewed scientific journals. His research areas include radar imaging, synthetic aperture radar (SAR), signal processing, electromagnetic scattering models, and remote sensing applications.

Dr. Ulander was the recipient of the Thulin Medal in silver from the Swedish Society of Aeronautics and Astronautics in 2020 and the Royal Swedish Academy of Engineering Sciences (IVA) for pioneering work of importance for ESA's BIOMASS mission.